Independent Component Analysis for the Multitag Detection of Frequency-Coded Chipless RFID

Wen-Sen Li, Cong-Zhi Peng, Fei-Peng Lai, Pin-Sung Lai, and Yen-Sheng Chen, *Member, IEEE*

***Abstract*— A multitag detection technique is proposed for frequency-coded chipless radio frequency identification (RFID) to achieve minimum separations of tags, enhanced data capacity, and calibration-free features. Previous attempts for multitag detection include signal processing, comparisons with a database, and space-division multiple access (SDMA); nevertheless, these techniques rise to the challenges of large separations of tags, reduced capacity, and the complexity due to a phased array or beamforming technology, respectively. In contrast, the proposed technique overcomes these limitations by a new framework that integrates signal processing and SDMA. The capability is derived from the independent component analysis (ICA), which transforms mixing backscattering fields into an optimization model; by using the Newton method to maximize non-Gaussianity, the original resonances of each tag can be recovered. Furthermore, the proposed technique eliminates the procedure of calibration. An 8 bit system is designed and tested over 2.0–5.0 GHz. When two tags are separated by 0, 10, and 20 mm, ICA shows average reliability of 80.4%, 90.4%, and 91.5%, respectively. Thus, closely adjacent tags can be detected without calibration even for a high-density system. Real-world implementation issues, including four-tag detection, orientation mismatch, and a displacement of tags, are also analyzed to validate the proposed technique.**

***Index Terms*— Collision avoidance, independent component analysis (ICA), radar cross sections, radio frequency identification (RFID), RFID tags.**

I. Introduction

CHIPLESS radio frequency identification (RFID) is considered a revolutionary communication system for automatic identification and data capture (AIDC). The tags of chipless RFID eliminate the use of microchips and develop the structure in a fully printable manner, thereby reducing the manufacturing cost compared to conventional ultrahigh-frequency (UHF) RFID. For the detection of one single tag, chipless RFID encodes and captures data through frequency [1]–[8], time [9]–[12], phase [13], or hybrid mechanisms [14]–[16]. However, when multiple tags are present, these encoding schemes suffer from the collision of data signature, causing confounding responses and signal interferences. In UHF RFID, the collision of multiple tags is resolved by protocols, such as time-division multiple access (TDMA) [17] and adaptive structuring of binary search trees [18]. These anticollision protocols are compiled in a medium access control (MAC) layer, implemented in the baseband module of a microchip. Nevertheless, as the microchip is removed, chipless tags cannot receive ternary feedback from a reader and take action accordingly. Thus, chipless RFID encounters severe difficulty in collision avoidance.

Earlier studies have presented multitag detection techniques for the frequency-coded chipless RFID [19]–[38]. The strategy can be classified into three types, including signal processing [19]–[30], the comparison of resonances with a database [31]–[35], and space-division multiple access (SDMA) [36]–[38]. First, signal processing is prevailing in the literature. This scheme transmits various forms of signals, investigating the time difference of arrivals (TDoA) using a specific scheme and determining the resonances accordingly. More specifically, the short-time matrix pencil method (STMPM) transmits frequency-modulated continuous-wave (FMCW) signals over 3.1–10.6 GHz to catch complex natural resonances based on the turn-on times of poles [19]–[21]. The fractional Fourier transform (FrFT) transmits linear frequency-modulated (LFM) signals and rotates the backscattering signals on a fractional domain [22]–[26]. The number of spikes on the fractional domain illustrates the number of tags collided and the associated TDoA, which enables the reader to separate signals and decode IDs. Other signal processing methods include FMCW radar [27], [28] and ultrawideband (UWB) impulse radio (IR) radar [29], [30]. However, the performance of these signal processing techniques relies on sufficient TDoA, which further imposes a constraint to the separation of tags.

The second multitag detection technique is based on the comparison of resonances with a database [31]–[35]. For example, the notch position modulation designs a system that has an additional preamble frequency and subfrequency bands. A reader detects the unique frequency shift of tags and compares the result with a database, thereby identifying the number of tags in the interrogation zone and the IDs [31]–[33]. A successive approximation comparative (SAC) scheme compares the amplitude of the backscattering signal with the database [34]. A lookup table approach encodes data at one resonant frequency. Assuming no mutual coupling, the envelope of the frequency responses indicates the number of tags collided and the associated IDs [35]. However, the challenge of these techniques is reduced data capacity. Several frequency slots are not encoded with actual

Manuscript received 10 August 2021; revised 5 December 2021; accepted 17 February 2022. Date of publication 28 March 2022; date of current version 8 September 2022. This work was supported by the Ministry of Science and Technology, Taiwan, under Contract MOST 110-2636-E-027-003. *(Corresponding author: Yen-Sheng Chen.)*

The authors are with the Department of Electronic Engineering, National Taipei University of Technology, Taipei 10608, Taiwan (e-mail: yschen@ntut.edu.tw).

Color versions of one or more figures in this article are available at https://doi.org/10.1109/TAP.2022.3161483.

Digital Object Identifier 10.1109/TAP.2022.3161483

information [31]–[33], or only one resonator is implemented for a tag [35]. This limits their information-carrying capability.

The third multitag detection technique is SDMA [36]–[38]. This technique has the highest implementation complexity and cost, as the reader architecture consists of a phased antenna array or beam-switching antennas. Such antennas create main beams with a narrow half-power beamwidth (HPBW), scanning the interrogation zone and performing one-by-one detection with reduced collision probability. However, the performance is sensitive to the HPBW. When multiple tags are found within the HPBW, SDMA may fail to separate the IDs.

In this article, a new multitag detection framework is proposed to improve the limitations of the earlier methods. The proposed technique is based on independent component analysis (ICA) [39], integrating the signal processing and SDMA into a systematic method. The kernel of the proposed technique, ICA, performs N measurements for N tags. Although the N samples are mixing and confounding information, ICA determines the optimum weights of the mixing backscattering fields to generate original resonances. Five distinctive features are observed for the proposed technique. First, the proposed technique requires no information regarding TDoA, thereby identifying multiple tags even for closely spaced scenarios. Second, the proposed method shows the potential for capacity enhancement, as it does not impose constraints on the arrangement of frequency slots. Third, the proposed technique does not require pairing with a reader antenna with a narrow HPBW; in contrast, by switching the main beam that shows a broad HPBW, the proposed technique can solve the mixing data more efficiently. Fourth, the ICA algorithm is not sensitive to prior knowledge or parameter setup, so it provides robust performance without subjective judgment. Finally, the proposed technique is the first multitag detection method that operates in a calibration-free manner. We integrate the short-time Fourier transform (STFT) into the process [40], [41], thereby eliminating the additional measurement of clutter.

In what follows, the theory and implementation of the technique are elaborated first. The procedure and distinct characteristics are described in detail. Subsequently, an 8 bit system to test the proposed technique is illustrated. Furthermore, while earlier studies investigate the anticollision techniques through specific cases, we evaluate the reliability in a statistical manner. The performance of the proposed technique is compared to the signal processing using STMPM and SDMA. Finally, the real-world issues of the proposed technique are analyzed. The detection performance of four collided tags, the effect of orientation mismatch, and the influence of a displacement of tags will be discussed.

II. Proposed Technique

The proposed technique is a hybrid method of signal processing and SDMA. This unique framework is derived from ICA, which is a computational method for separating mixing signals into additive individuals, assuming that the individual components are non-Gaussian and statistically independent. ICA has been applied to a wide sphere of signal processing, such as biomedical technology, telecommunications, and the prediction of stock market prices. In the multitag detection problem, the goal is to separate a mixture of multiple resonances. Our preliminary results indicate that the backscattering field does not follow Gaussian distribution, illustrated from the quantile–quantile (Q-Q) plot of normalized radar cross section (RCS). Furthermore, as the induced current of a resonator resulting from adjacent tags is generally weak, the insignificant mutual coupling suggests the low correlation of backscattering fields. These characteristics show that the multitag detection problem suits the framework of ICA.

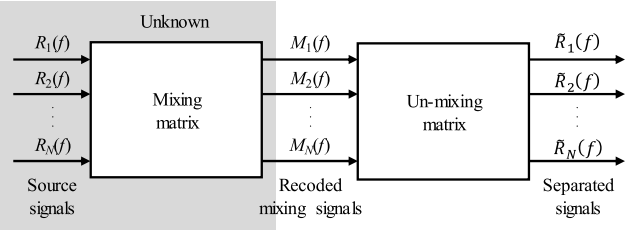

Fig. 1. Block diagram of blind source separation for a mixture of backscattering signals.

The concept of the proposed framework is graphically illustrated in Fig. 1. Considering N tags under test, the cross-polarized backscattering response of which is denoted by $R_i(f)$, where f is frequency and index $i = 1, 2, \ldots, N$, reading their joint responses causes confounding frequency signatures, denoted by $M_i(f)$. To separate these mixing signals, the proposed technique requires performing N tests that sample each $M_i(f)$. The proposed technique aims to determine an un-mixing matrix and generate the estimation of the original source signals, denoted by $\tilde{R}_i(f)$, from the N mixing signals.

The flowchart of the proposed technique is shown in Fig. 2. First, the proposed technique performs the time–frequency analysis to prevent measuring the response of clutter. The confounding signals $M_i(f)$ is converted using the inverse fast Fourier transform (IFFT), leading to a mixture of time-domain signals, denoted by $s_i(t)$, where t is the time. As $s_i(t)$ consists of the reflection of the input port of a reader antenna, the response of tags, and the response of clutter, a window characterized by $w(t)$ is implemented to filter undesired segments. Next, the time-domain signal $s_i(t)$ is converted into a time–frequency spectrogram using STFT

$$S_i(f, \tau) = \int_{-\infty}^{+\infty} s_i(t) w(\tau - t) \mathrm{e}^{-j2\pi f t} \mathrm{d}t \tag{1}$$

where $S_i(f, \tau)$ is the signal as the function of both time and frequency, and τ is delay time across $w(t)$. The window function $w(t)$ is implemented as a Hamming window with a length of 21.7 ns. Considering sample size of frequency count, C_f, and time count, C_t, $S_i(f, \tau)$ depicts dimensions of $C_f \times C_t$.

Although $S_i(f, \tau)$ is the signal implemented by ICA, they are averaged over all potential τ, resulting in a frequency response that characterizes resonances, denoted by $K_i(f)$. This performance index is employed to recognize whether

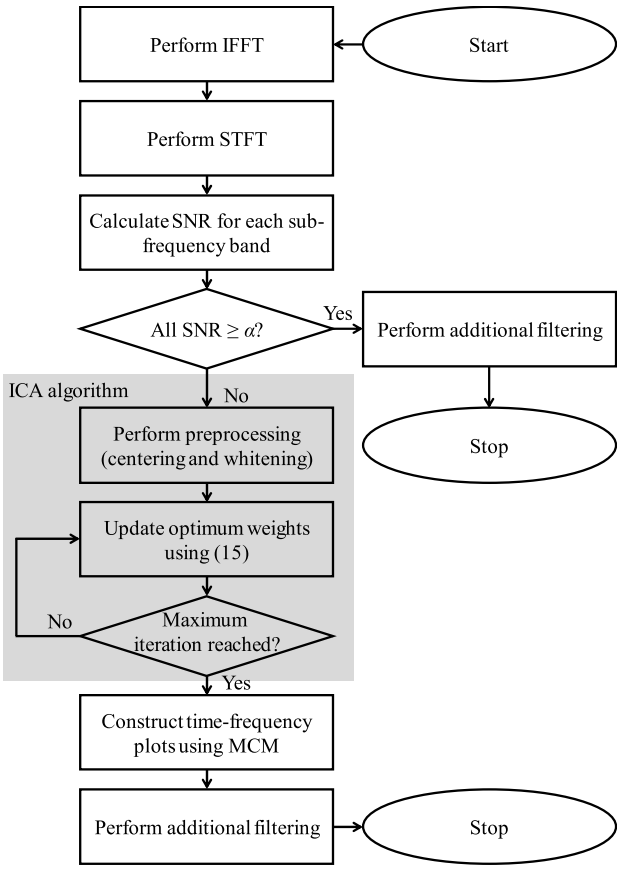

Fig. 2. Flowchart of the proposed technique integrating with STFT.

collisions occur. When only one tag locates within the HPBW of a reader antenna, bypassing the ICA algorithm can speed up the procedure, and the detection process is reduced to SDMA. The recognition of collisions is performed through the signal-to-noise ratio (SNR) over each subfrequency band. Considering a frequency shift encoding system [42], the parameters of which include Q subfrequency bands and R frequency slots in a subfrequency band, the proposed technique evaluates SNR in the jth subfrequency band as

$$\mathrm{SNR}_j = \frac{A_i^{max}(f)_j}{A_i^{sl}(f)_j} \tag{2}$$

where $A_i^{max}(f)_j$ and $A_i^{sl}(f)_j$ are the maximum and second-largest amplitudes among R frequency slots, respectively, and index $j = 1, 2, \ldots, Q$. Following this definition, SNR_j is always greater than 0 dB. A high SNR_i denotes only one significant resonance in the jth subfrequency band; in contrast, SNR_j approaching 0 dB indicates multiple resonances, which further suggests that a collision happens, and the backscattering fields are caused by a mixture of collided IDs. If $\mathrm{SNR}_j \geq \alpha$ for all the Q subfrequency bands, the proposed technique bypasses the ICA algorithm and outputs the IDs immediately, where α is a threshold adaptively controlled below 2.6 dB. Otherwise, the proposed technique evaluates the measured results as a collision problem.

The collision problem is the kernel of this study. The statistics for the ICA algorithm are the confounding signals $S_i(f, \tau)$ at each τ. To better explain the mathematical development, these confounding signals are cast into a matrix, $\mathbf{S}(\tau)$

$$\mathbf{S}(\tau) = \begin{bmatrix} S_1(f,\tau) & \ldots & S_N(f,\tau) \end{bmatrix}^T \tag{3}$$

where each column consists of elements sampled at f. Thus, the dimensions of $\mathbf{S}(\tau)$ are $N \times C_f$.

Before executing the ICA computation, $\mathbf{S}(\tau)$ requires preprocessing including centering and whitening. The column of $\mathbf{S}(\tau)$ is centered to zero by subtracting the average frequency response, denoted by $\bar{S}_i(\tau)$. This provides ICA with a measure with zero mean, expressed as $\mathbf{S}_C(\tau)$

$$\mathbf{S}_C(\tau) = \begin{bmatrix} S_1(f,\tau) - \bar{S}_1(\tau) & \ldots & S_N(f,\tau) - \bar{S}_N(\tau) \end{bmatrix}^T. \tag{4}$$

Next, we perform eigenvalue decomposition (EVD) to the covariance matrix of $\mathbf{S}_C(\tau)$ denoted by $E\{\mathbf{S}_C(\tau)\mathbf{S}_C^T(\tau)\}$ [39]

$$E\left\{\mathbf{S}_C(\tau)\mathbf{S}_C^T(\tau)\right\} = \mathbf{V}\mathbf{D}\mathbf{V}^T \tag{5}$$

where $\mathbf{V}$ is the matrix comprised of the eigenvectors of the covariance matrix and $\mathbf{D}$ is the diagonal matrix of the eigenvalues. The data executing ICA is transformed as

$$\mathbf{S}_w(\tau) = \mathbf{V}\mathbf{D}^{-\frac{1}{2}}\mathbf{V}^T\mathbf{S}_C(\tau). \tag{6}$$

Such an operation is characterized as whitening. As such, the vectors in $\mathbf{S}_w(\tau)$ are uncorrelated and have unit variance.

For simplification purposes, we eliminate the function notation of τ. $\mathbf{S}_w$ is treated as the mixing matrix, and the goal of ICA is to determine decision variables, $\mathbf{w}$, that maximize the non-Gaussianity indicator, ζ_G

$$\begin{aligned} &Max.\ \zeta_G(\mathbf{w}) = E\left\{G\left(\left|\mathbf{w}^H\mathbf{S}_w\right|^2\right)\right\} \\ &s.t.\ E\left\{\left|\mathbf{w}^H\mathbf{S}_w\right|^2\right\} = \|\mathbf{w}\|^2 = 1 \end{aligned} \tag{7}$$

where G is the one-unit contrast function. While G has several choices [43], this study selects the following expression as the contrast function:

$$G(y) = \frac{1}{2}y^2 \tag{8}$$

which makes the objective function a quartic function. Such a selection develops the objective function into the "Kurtosis" of an argument, which denotes the non-Gaussianity of the combination of $\mathbf{S}_w$. When the Kurtosis is zero, the distribution of the mixing data is exactly Gaussian. In other words, the optimization problem shown in (7) aims to maximize the non-Gaussianity of the mixing data $\mathbf{S}_w$.

To cope with the nonlinear programming problem as (7), it is necessary to examine the problem nature by the Karush–Kuhn–Tucker (KKT) conditions [44], which indicates that the optima of the objective function are determined at points where

$$\nabla E\left\{G\left(\left|\mathbf{w}^H\mathbf{S}_w\right|^2\right)\right\} - C\nabla E\left\{\left|\mathbf{w}^H\mathbf{S}_w\right|^2\right\} = 0 \tag{9}$$

where C is a real constant and ∇ is the gradient. As the backscattering fields of frequency-coded chipless tags are complex numbers, the operation of the gradient requires separating the real and imaginary parts of (9), leading to

$$E\left\{2\mathbf{S}_w\left(\mathbf{w}^H\mathbf{S}_w\right)^* G'\left(\left|\mathbf{w}^H\mathbf{S}_w\right|^2\right)\right\} - 2C\mathbf{w} = 0 \tag{10}$$

where G' is the derivative of the contrast function. To obtain an explicit expression for $\mathbf{w}$, we apply the Newton method to solve (10). By separating the expectations and approximating $E\{\mathbf{S}_w\mathbf{S}_w^H\}$ as zero, the Jacobian matrix of $\nabla E\{|\mathbf{w}^H\mathbf{S}_w|^2\}$ can be expressed as

$$\nabla^2 E\left\{G\left(\left|\mathbf{w}^H\mathbf{S}_w\right|^2\right)\right\} \approx 2E\left\{G'\left(\left|\mathbf{w}^H\mathbf{S}_w\right|^2\right)+\left|\mathbf{w}^H\mathbf{S}_w\right|^2 G''\left(\left|\mathbf{w}^H\mathbf{S}_w\right|^2\right)\right\}\mathbf{I} \quad (11)$$

where G'' is the second-order derivative of the contrast function and $\mathbf{I}$ is the identity matrix. Similarly, the Jacobian matrix of $C\nabla E\{|\mathbf{w}^H\mathbf{S}_w|^2\}$ is

$$C\nabla^2 E\left\{\left|\mathbf{w}^H\mathbf{S}_w\right|^2\right\} = 2C\mathbf{I} \quad (12)$$

which introduces the total Jacobian, $\mathbf{J}$, of (9)

$$\mathbf{J}=2E\left\{G'\left(\left|\mathbf{w}^H\mathbf{S}_w\right|^2\right)+\left|\mathbf{w}^H\mathbf{S}_w\right|^2 G''\left(\left|\mathbf{w}^H\mathbf{S}_w\right|^2\right)-C\right\}\mathbf{I}. \quad (13)$$

$\mathbf{J}$ is a diagonal matrix. The resultant Newton iteration becomes

$$\mathbf{w}_{k+1}=\mathbf{w}_k-\frac{E\left\{\mathbf{S}_w\left(\mathbf{w}_k^H\mathbf{S}_w\right)^* G'\left(\left|\mathbf{w}_k^H\mathbf{S}_w\right|^2\right)\right\}-C\mathbf{w}_k}{E\left\{G'\left(\left|\mathbf{w}_k^H\mathbf{S}_w\right|^2\right)+\left|\mathbf{w}_k^H\mathbf{S}_w\right|^2 G''\left(\left|\mathbf{w}_k^H\mathbf{S}_w\right|^2\right)\right\}-C} \quad (14)$$

where $\mathbf{w}_{k+1}$ and $\mathbf{w}_k$ denote the decision variables for the $(k+1)$th and kth iterations, respectively. Finally, multiplying the both sides by $C - E\{G'(|\mathbf{w}_k^H\mathbf{S}_w|^2) + |\mathbf{w}_k^H\mathbf{S}_w|^2 G''(|\mathbf{w}_k^H\mathbf{S}_w|^2)\}$ produces the update equation of the decision variables

$$\mathbf{w}_{k+1} = E\left\{\mathbf{S}_w\left(\mathbf{w}_k{}^H\mathbf{S}_w\right)^* G'\left(\left|\mathbf{w}_k{}^H\mathbf{S}_w\right|^2\right)\right\} -E\left\{G'\left(\left|\mathbf{w}_k{}^H\mathbf{S}_w\right|^2\right)+\left|\mathbf{w}_k{}^H\mathbf{S}_w\right|^2 G''\left(\left|\mathbf{w}_k{}^H\mathbf{S}_w\right|^2\right)\right\}\mathbf{w}_k. \quad (15)$$

The convergence condition for (15) is the maximum number of iterations. The resultant optimum weights, denoted by $\tilde{\mathbf{w}}$, are multiplied by the mixing sources, generating a matrix that consists of the individual resonances at each τ, denoted by $\tilde{\mathbf{R}}(\tau)$

$$\tilde{\mathbf{R}}(\tau) = \tilde{\mathbf{w}}^H\mathbf{S}_w \quad (16)$$

where the row of $\tilde{\mathbf{R}}(\tau)$ is the independent frequency response of tags.

The ICA algorithm repeats for C_t times. When the estimated resonances are obtained for all the τ, they are combined into the time–frequency plot of separated signals. However, ICA depicts a limitation of permutation ambiguity. The order of the estimated separated resonances is inconsistent. This challenge is addressed using the maximum correlation method (MCM). A succeeding segment is connected to the previous one with the maximum correlation. This results in the estimated time–frequency plot of independent components. Finally, averaging the magnitudes over τ brings the frequency response that comprises resonance information; by performing additional filtering [41], clear and separated frequency signatures, $\tilde{R}_i(f)$, are, thus, determined for the N tags.

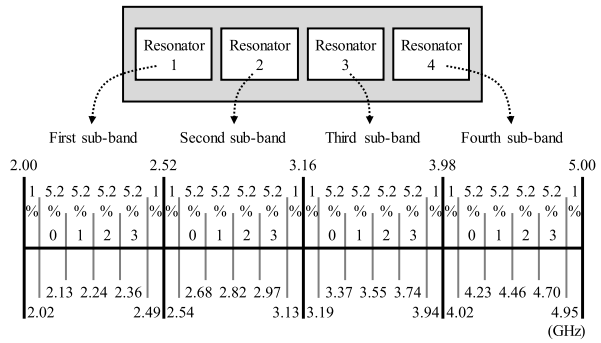

Fig. 3. Frequency spectrum of the 8 bit frequency-coded chipless RFID system.

III. System Setup

To validate the proposed technique at a system level, we design an 8 bit frequency-coded chipless RFID over 2.0–5.0 GH. For comparison purposes, signal processing using STMPM and SDMA is also developed and tested.

A. Implementation of an 8 bit System

Fig. 3 demonstrates the frequency spectrum of the 8 bit system. This chipless RFID employs frequency shift encoding, the parameters of which are five subfrequency bands ($Q = 4$) and four frequency slots ($R = 4$). An important characteristic of this system is the prevention of fixed bandwidths in a linear-scale system. The fixed frequency range at a relatively high frequency causes a smaller fractional bandwidth, which further incurs a smaller margin of detection errors and the unfair evaluation of reliability [45]. The frequency ranges of the four subfrequency bands are 2.00–2.52, 2.52–3.16, 3.16–3.98, and 3.98–5.00 GHz, respectively, whereas the fractional bandwidths are all 22.8%. Each subfrequency band consists of four frequency slots and two guardbands. The frequency slots have a fractional bandwidth of 5.2%, whereas the guardbands depict a fractional bandwidth of 1.0%.

The proposed system employs a broad bandwidth of over 2.00–5.00 GHz. If the bandwidth is reduced by 50%, the frequency shift of a resonance caused by manufacturing errors and the loading effect of the environment may incur false detection. To clarify the contributor of the false detection, this broad bandwidth is implemented so that the evaluation of reliability can focus on the anticollision techniques.

This frequency shift encoding system creates $4^4 = 256$ combinations of IDs, namely, a data capacity of 8 bits. This capacity is higher than the ones in the previous studies demonstrating multitag detection methods [19]–[38].

B. Tag Design

To accommodate the 8 bit detection system, a chipless tag that comprises four resonators is designed, as shown in Fig. 4. The resonator is five thin strips oriented at 45° and backed with a conductor [40]. These thin strips are printed on a 0.813 mm-thick RO4003C substrate (dielectric constant $\varepsilon_r = 3.55$ and loss tangent $\tan\delta = 0.0027$), the dimensions of which are 85.0 mm × 40.0 mm.

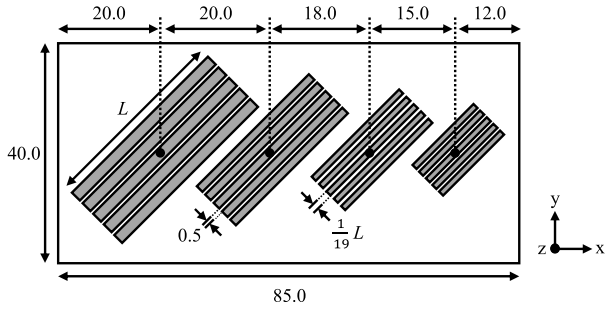

Fig. 4. Configuration of the chipless tag that validates the proposed technique (unit: mm).

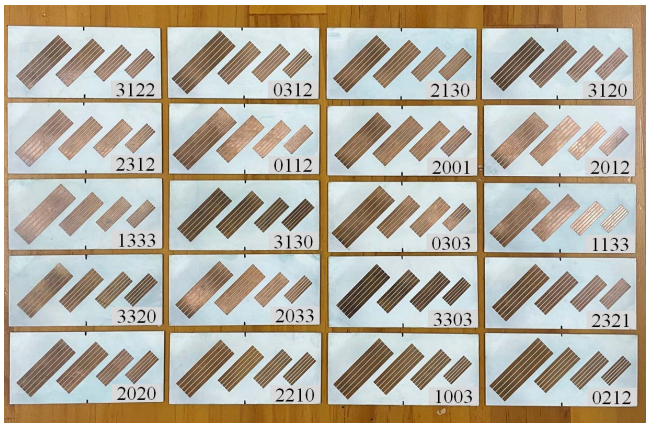

Fig. 5. Test pieces of the chipless RFID tags.

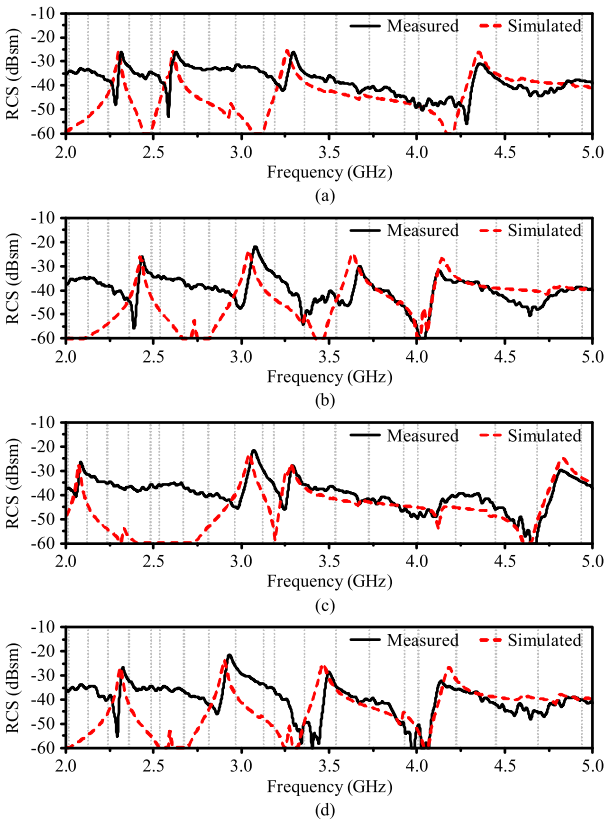

Fig. 6. Simulated and measured RCS responses for tags with IDs of (a) 2001, (b) 3320, (c) 0303, and (d) 2210.

The phase center of the four resonators aligns horizontally. The separations between the adjacent phase centers are 20.0, 18.0, and 15.0 mm, respectively. When the tag is illuminated by y-polarized plane waves, the resonant frequency of the x-polarized backscattering fields can be controlled by tuning the length of the strips. The resonant frequency is defined as the one that shows the maximum receiving amplitude among the four frequency slots. In addition, the gap between two adjacent strips is fixed as 0.5 mm, whereas the width of the strips is set to 1/19 times the associated length, denoted by L. These chipless tags are designed using HFSS simulation. In particular, 20 tags are randomly selected and fabricated. The photograph of these test pieces is shown in Fig. 5. As an example, the simulated and measured RCS responses of four tags, including 2001, 3320, 0303, and 2210, are shown in Fig. 6. We use a quaternary system to record the IDs, as this representation can illustrate the resonant frequencies more conveniently. The measured results agree well with the simulated ones, thereby validating the design principle.

Note that the proposed technique is independent of the topology of the tag, subject to cross-polarized encoding.

C. Reader

The proposed technique can be applied to the reader transmitting FMCW signals. Fig. 7 depicts the reader architecture of the proposed technique. While the transceiver follows the ones in earlier studies [46], [47], the antenna should be able to take multiple samples of mixture signals. While relocating the

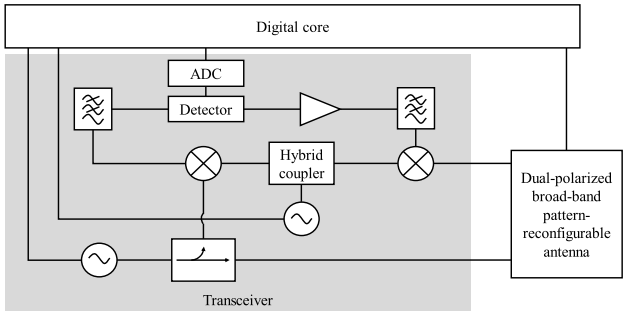

Fig. 7. Architecture of the reader that serves the proposed technique.

reader can create multiple samples, this scheme is impractical in real-world applications; thus, the reader is equipped with a pattern-reconfigurable antenna with broad HPBWs. This characteristic reduces the hardware complexity, size, and costs from SDMA, the deployment of which is a phased array antenna with narrow agile beams. The phased array antenna is developed into beam steering or beamforming, which requires an additional power divider and phase shifters. In contrast, the proposed technique has the capability of blind source separation, thereby eliminating the use of a beamforming network.

Fig. 8 depicts the experimental setup for the chipless RFID system. The reader transceiver employs a vector network analyzer PNA N5227A from Keysight, and the pattern-reconfigurable antenna is implemented as a horn

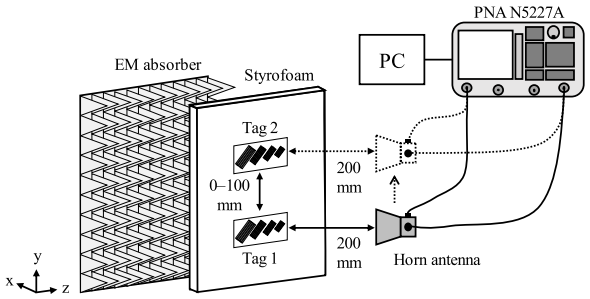

Fig. 8. Experimental setup for testing the proposed technique and SDMA.

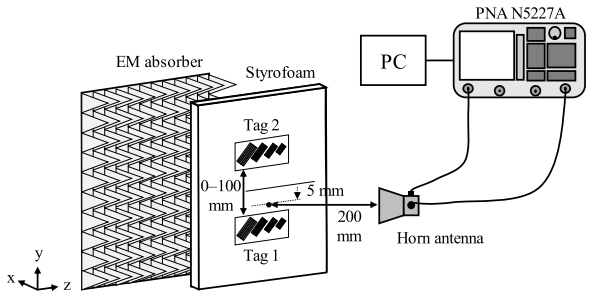

Fig. 9. Experimental setup for testing STMPM.

antenna covering 2.0–18.0 GHz, the pattern of which is controlled manually. In 2.0–5.0 GHz, the HPBW of the horn antenna on the E- and H-planes are 33.3°–61.9° and 46.6°–68.4°, respectively. The demonstration of the proposed technique will be the scenarios where multiple tags have collided responses. The separation of chipless tags, denoted by d, ranges from $d = 0$ mm to $d = 100$ mm with incremental steps of 10 mm. The horn antenna illuminates the phase center of each tag with a read range of 200 mm, measuring the backscattering, potentially mixture signals. These signals are processed using the proposed technique, which finally outputs the original and individual tag responses.

D. STMPM and SDMA

Before we demonstrate the results of the proposed technique, two state-of-the-art multitag detection methods, including STMPM and SDMA, are implemented for comparison purposes.

Considering that multiple tags are present, STMPM first performs calibration to subtract the effect of clutter. The mixture backscattering signals of the tags are measured in terms of frequency-domain responses, which are readily converted into time-domain signals. The kernel of STMPM is to extract poles and residues from time–frequency and space–frequency diagrams, respectively [19]–[21], which provides estimations on the complex natural resonances and turn-on time of individual tags. The accuracy of the estimation relies on prior knowledge about the number of significant decimal digits, denoted by P, and the window's length that distinguishes resonances, denoted by T_w. In addition, the implementation of these parameters is related to the SNR in the environment. As a narrower separation of tags incurs lower SNR, the performance of STMPM is subject to the range resolution of tags.

The experimental setup of STMPM is shown in Fig. 9. The same horn antenna illuminates the vertical center of two tags offset by 5.0 mm, creating the TDoA for backscattering signals. The separation of two chipless tags and the read range are identical to those for testing ICA. The mixing backscattering signals are processed to extract the poles. The parameters used are adaptive P ranging from 4 to 8 and $T_w = 10^{-4}$ ns.

In the SDMA deployment, the experimental setup follows the test of the proposed technique excluding the ICA processing. As shown in Fig. 8, although various tags may enter the interrogation zone, the backscattering responses are read and decoded into IDs immediately.

IV. Results

The performance of the proposed technique, STMPM, and SDMA is examined by detection reliability. Reliability is defined as the probability that a reader successfully detects and identifies a chipless tag. This definition is strict to performance evaluation, as the error detection of only one digit ruins the result. For the 20 chipless tags fabricated, 30 combinations are randomly selected out of $C_2^{20} = 190$ ones. The mixture backscattering signals of the 30 combinations are measured for eight repeated tests. Summarizing 11 separations tested, 30 (combinations) $\times$ 11 (separations) $\times$ 8 (tests) $=$ 2640 measurements are carried out. In addition, another 2640 measurements are performed for testing STMPM, where the combinations of tags remain identical. Fig. 10 demonstrates the photographs of the experiment for testing the proposed technique.

A. Demonstration

First, the detection results for two tags with IDs of 2001 and 3320 are demonstrated. For explanation purposes, here, the performance index of backscattering fields is taken as RCS, which requires performing calibration for the clutter. Considering $d = 10.0$ mm, the TDoA of the two tags is only 0.04 ns, which requires extremely high resolution to separate them directly in the time domain. When the horn antenna illuminates the tags with IDs of 2001 and 3320, respectively, the RCS responses are depicted in Fig. 11(a) and (b). In comparison with the individual responses shown in Fig. 6(a) and (b), the four subfrequency bands depict multiple resonances with comparable amplitudes, which causes an incorrect evaluation for IDs. The IDs are decoded as 3300 and 2301, respectively. This confirms the limitation of SDMA.

The proposed technique is applied to separate the mixture signals. Fig. 12 shows the iteration history of Kurtosis, which reaches the maximum after the seventh iteration. The optimum weights for the two mixing backscattering signals are

$$\tilde{\mathbf{w}} = \begin{bmatrix} -0.52 - j0.24 & -0.57 - j0.59 \\ 0.17 - j0.80 & -0.31 + j0.48 \end{bmatrix}. \quad (17)$$

Fig. 12 also depicts the iteration history for other separations. The results indicate fast convergences for all the scenarios.

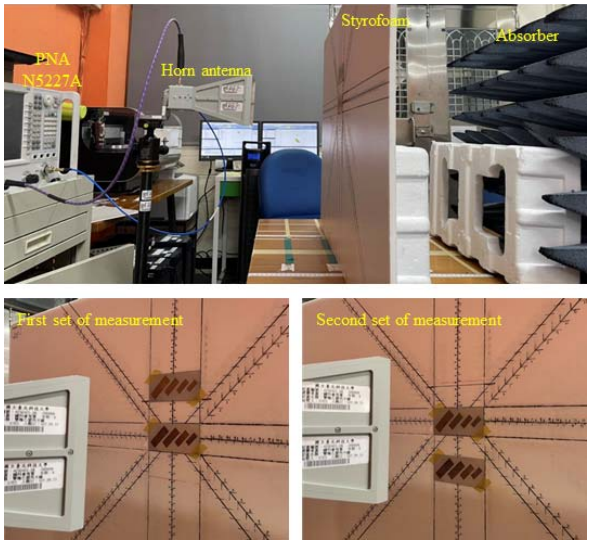

Fig. 10. Photographs of the experiment for separating mixture backscattering signals.

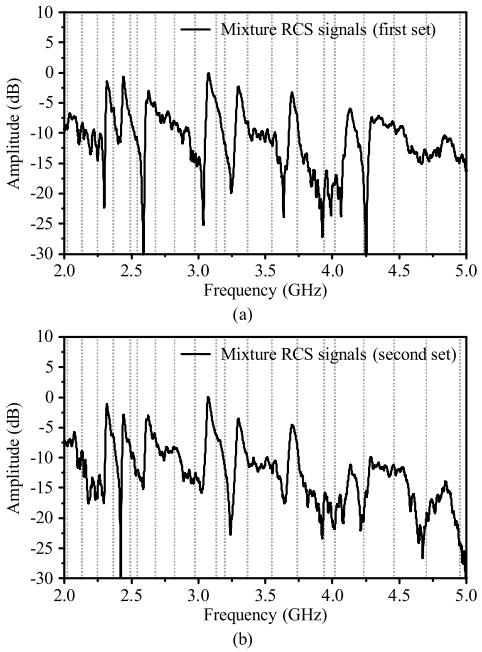

Fig. 11. Mixture RCS responses detected by SDMA as the horn antenna illuminates the tags with IDs of (a) 2001 and (b) 3320.

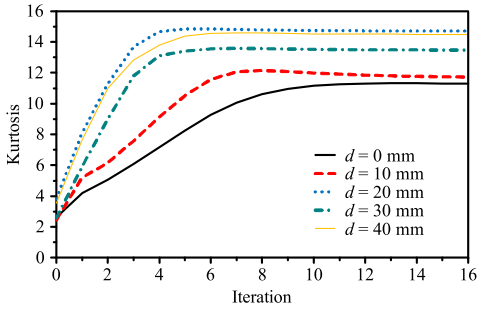

Fig. 12. Iteration history of Kurtosis for various separations.

To demonstrate the process of blind source separation, the decision variables at the third, sixth, and (17) are substituted into (16), and the resultant separated frequency responses are shown in Fig. 13. In each subfrequency band, the multiple resonances gradually vanish, thereby introducing a clarified interpretation on the frequency slot that depicts unique maximum amplitude.

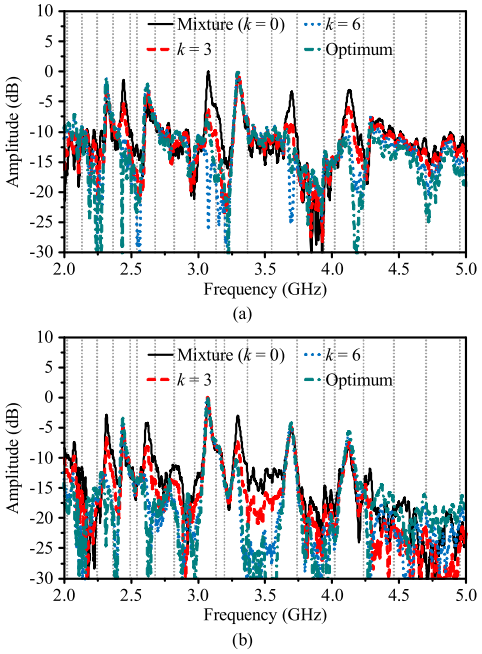

Fig. 13. Separated RCS responses for various iterations. (a) First mixture, gradually evolving into 2001. (b) Second mixture, gradually evolving into 3320.

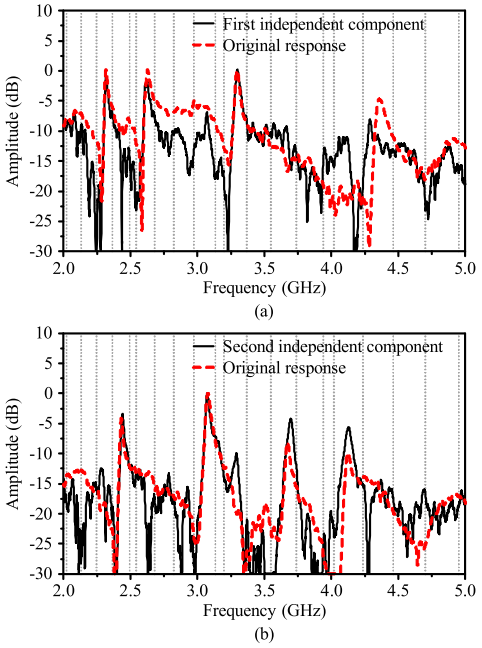

Fig. 14. Separated RCS responses for the tags with IDs of (a) 2001 and (b) 3320.

As the Newton method converges, the separated responses for the mixture signals are shown in Fig. 14. The original normalized RCS of one single tag is also illustrated in Fig. 14. This indicates that the individual frequency signatures are successfully recovered by the proposed technique even for $d = 10.0$ mm.

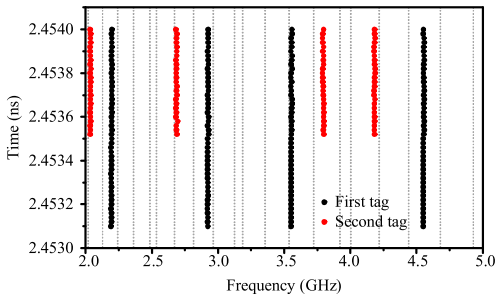

Fig. 15. Multitag detection using STMPM for the tags with IDs of 2001 and 3320.

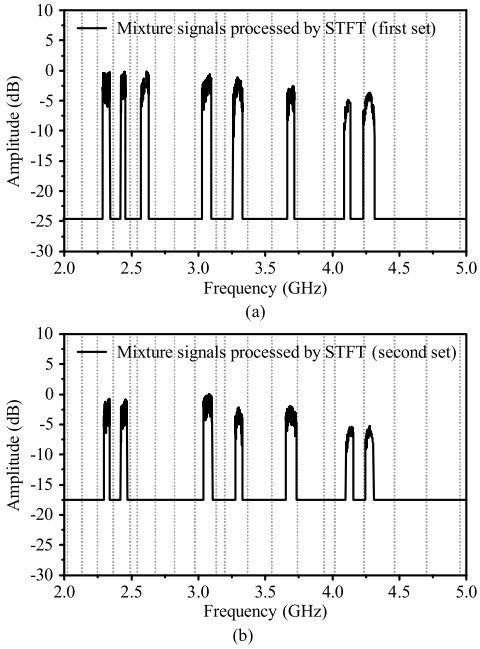

Fig. 16. Mixture detection results using the calibration-free SDMA for the tags with IDs of (a) 2001 and (b) 3320.

In contrast, the detection results of STMPM are shown in Fig. 15. The time–frequency plot is implemented to observe the signals. The early time components converge at 2.4531 and 2.4535 ns, where the turn-on time separates the complex natural resonances of the two tags. However, this early time is so small that the two backscattering signals cannot be separated clearly. The IDs of the first and second tags are decoded as 1222 and 0130, respectively, which cannot provide the correct output.

Next, the proposed technique with the calibration-free feature is demonstrated. Considering the same scenario, Fig. 16(a) and (b) presents the mixing signals when the horn antenna illuminates the tags with $d = 10.0$ mm. These results depict unclear evaluations as those in Fig. 11. Multiple local maxima occur even though a filtering mechanism has been implemented, as the collided responses have comparable magnitudes. The IDs are output as 3001 and 2321, respectively.

To apply the proposed technique to backscattering fields manipulated by STFT, the segments of the mixture signals before filtering are processed. Following the procedure shown

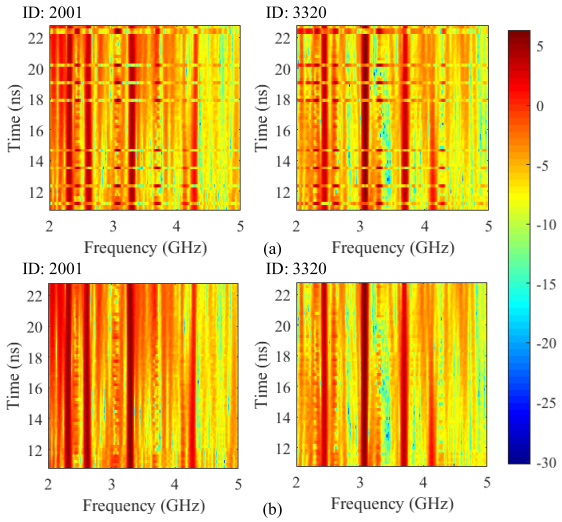

Fig. 17. Time–frequency plots using STFT for the tags with IDs of 2001 and 3320. (a) Before and (b) after reorganization using MCM.

in Fig. 2, these segments perform centering, whitening, mathematical model solving, and data reorganization using MCM. In particular, Fig. 17 explains the operation toward segments at each τ and the necessity of performing MCM. The delay time is sampled into 63 segments that operate ICA independently. Due to the permutation ambiguity of the ICA, the orders of the resultant segments have been reversed at several times, as shown in Fig. 17(a). Thus, the proposed technique employs MCM to recover the correct order. As a result, Fig. 17(b) illustrates the estimated time–frequency plots of the separated responses. Nevertheless, operating ICA for each delay segment makes the detection process time-consuming. In terms of one group of the test, our computer (1.00 GHz processor with 8 GB of RAM) spends 0.53 and 0.03 s to perform the calibration-free ICA and the ICA using RCS as a performance index, respectively. This further points out that the elimination of the calibration cannot be obtained without the tradeoff of computational efforts.

Converting the time–frequency plots into frequency signatures, the separated responses after filtering are demonstrated in Fig. 18. The original normalized RCSs of the individual tags are also depicted. The proposed technique can not only recover the independent signals but it also develops more obvious distinctions to reveal resonant frequencies, which is helpful for improving reliability.

The second example is two tags with IDs of 0303 and 2210, the separation of which is $d = 0$ mm. In this scenario, the two tags are immediately adjacent to each other. The HPBW of the horn antenna cannot distinguish such a narrow separation, so the SDMA results in mixing RCS responses, as shown in Fig. 19. All the subfrequency bands have two peaks, leading to incorrect IDs (0310 and 2313). Similarly, using the calibration-free method depicts the same limitation. The SDMA results processed by STFT and filtering are shown in Fig. 20, which outputs incorrect IDs of 0300 and 2213.

These mixture results are addressed using the proposed technique. The convergence history indicates that the Kurtosis reaches the maximum after 12 iterations. The optimum

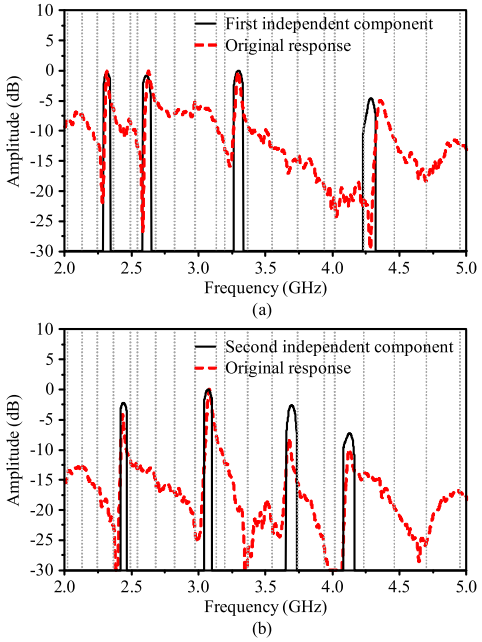

Fig. 18. Separated frequency signatures without performing calibration for the tags with IDs of (a) 2001 and (b) 3320.

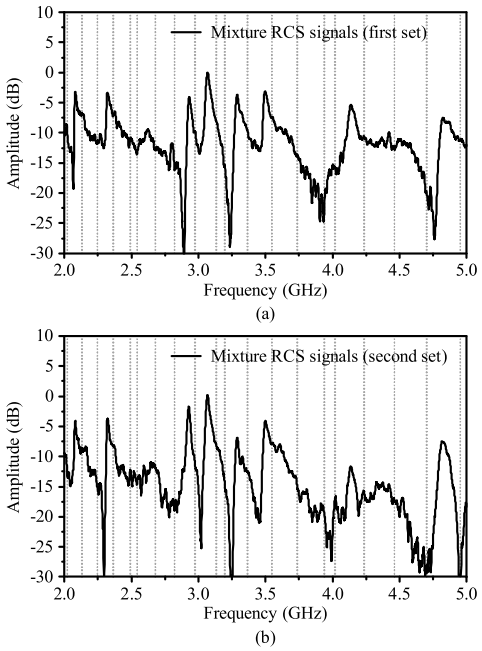

Fig. 19. Mixture RCS responses detected by SDMA as the horn antenna illuminates the tags with IDs of (a) 0303 and (b) 2210.

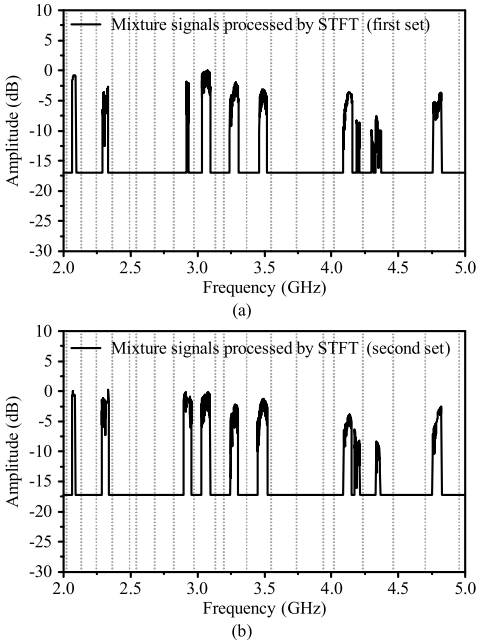

Fig. 20. Mixture detection results using the calibration-free SDMA for the tags with IDs of (a) 0303 and (b) 2210.

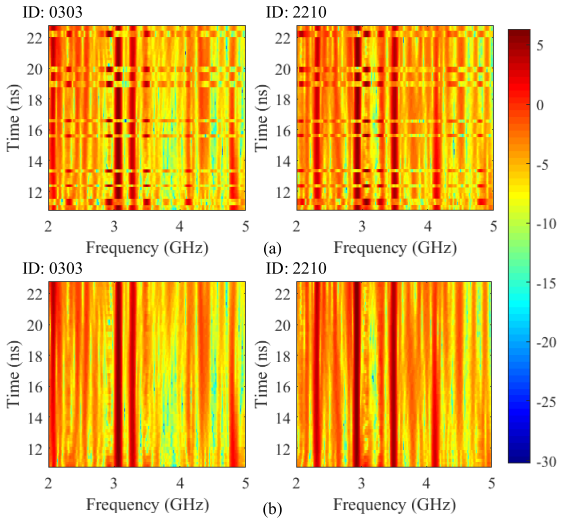

Fig. 21. Time–frequency plots using STFT for the tags with IDs of 0303 and 2210. (a) Before and (b) after reorganization using MCM.

weights multiplied by the mixture signals generate individual time–frequency components, as shown in Fig. 21(a). Finally, the rearranged segments shown in Fig. 21(b) lead to separated frequency signatures, as shown in Fig. 22. In comparison with the original responses shown in Fig. 6(c) and (d), the proposed technique successfully recovers the IDs without performing calibration.

B. Reliability

The results of all the $2640 \times 2 = 5280$ measurements are evaluated in terms of reliability. When RCS is treated as the backscattering signals, the detection reliability for ICA, STMPM, and SDMA is shown and compared in Fig. 23. The reliability of ICA is higher than 64.6%, where the lowest one appears at $d = 0$ mm. For $d \geq 10$ mm, the reliability is generally greater than 80%. In contrast, when small separations are the case ($d \leq 40$ mm), SDMA shows reliability ranging from 19.4% to 27.1%. STMPM has difficulty in these scenarios, where the reliability is lower than 12.1%. The reason is insufficient TDoA, which further causes ambiguity in separating the signals. When the separation increases ($d \geq 80$ mm), the reliability of SDMA is enhanced as 97.7%, as only one tag is found in the HPBW of the horn antenna. Nevertheless, ICA depicts similar performance as SDMA because of the stage of the SNR evaluation [see (2)]. However, the reliability

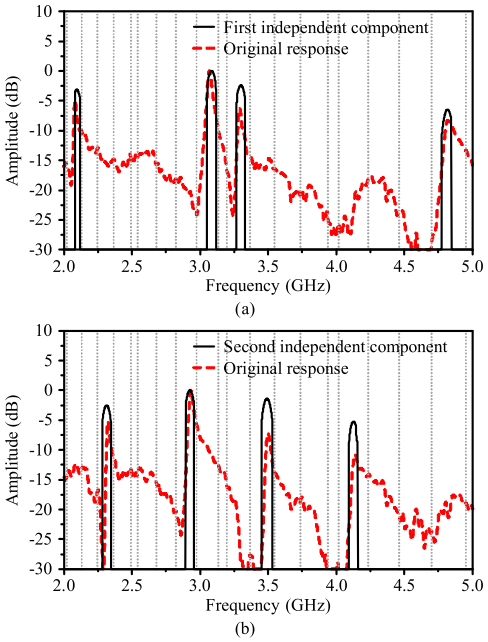

Fig. 22. Separated frequency signatures without performing calibration for the tags with IDs of (a) 0303 and (b) 2210.

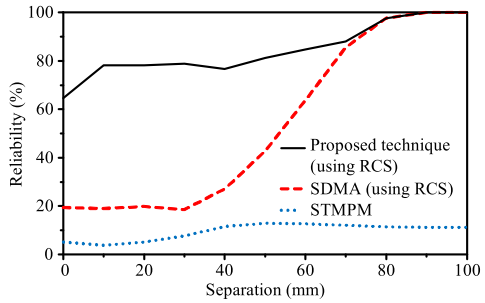

Fig. 23. Comparison of reliability using RCS as a frequency signature.

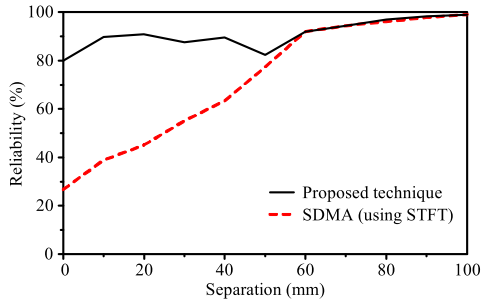

Fig. 24. Comparison of reliability with the calibration-free feature.

of STMPM is still limited to the resolution of TDoA. Note that the separations in the experiment are narrower than the minimum range resolution of STMPM, which is 70–150 mm at 3.1 GHz [19]. The performance evaluation of STMPM under such narrow separations is not standard; nevertheless, this challenging scenario is where ICA can demonstrate its distinct feature.

Moreover, when the clutter is eliminated using STFT, the comparison of reliability is shown in Fig. 24. Once again, the proposed technique outperforms SDMA in all the separations

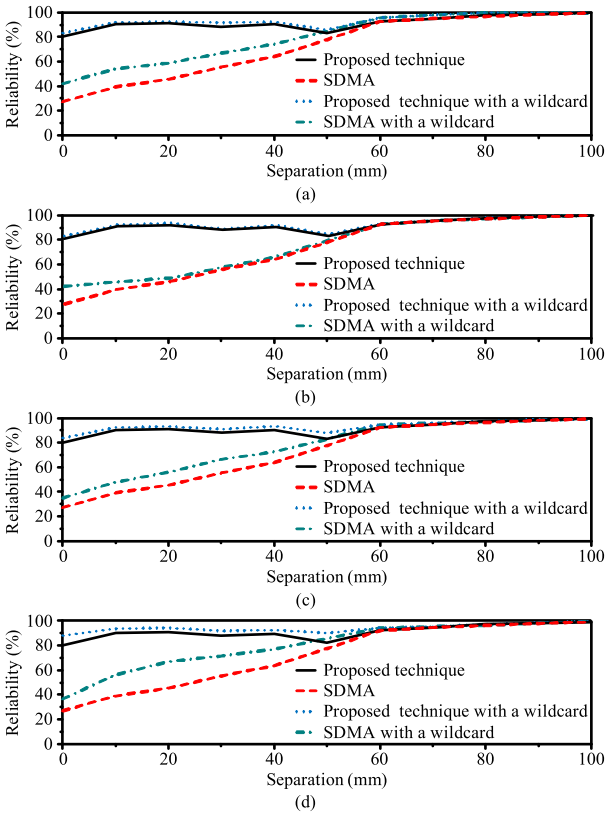

Fig. 25. Improvement of reliability when a wildcard is put to (a) first, (b) second, (c) third, and (d) fourth subfrequency bands.

considered. In particular, when $d \leq 30$ mm, the reliability of the proposed technique is 80.4%–90.5%, whereas that of the SDMA is 27.3%–55.6%. Improvements of 32.5%–53.1% are observed, showing that ICA is particularly suitable for separating mixing and confounding backscattering signals.

An interesting observation is that both the SDMA using STFT and the ICA integrated with STFT outperform the RCS versions, despite the fact that they remove the procedure of calibration. For $d \leq 40$ mm, the ICA integrated with STFT shows average reliability of 88.1%, whereas the ICA performing an additional run of calibration is only 75.3%; thus, the calibration-free feature integrated not only suits real-world applications but also enhances the reliability by 12.8%. Such improvements are achieved by additional filtering. The performance of STMPM is not included in this regard, as this scheme requires measuring the response of clutter.

C. Discussion

To examine the reliability obtained, we employ a wildcard character, "∗", for the resonance in each subfrequency band. When the wildcard character is put to a digit, this substring means that the error detection caused by that digit is permissible. For example, "03*3" denotes four substrings, including 0303, 0313, 0323, and 0333. If the reliability resulting from a one-character wildcard is improved significantly, that subfrequency band incurs more severe errors than other bands do.

Fig. 25 illustrates the results when the wildcard is put to each subfrequency band. The first and second subfrequency

TABLE I
COMPARISON OF CHARACTERISTICS FOR MULTITAG DETECTION METHODS

Issue	Proposed technique	Signal processing (STMPM)	SDMA	Comparison of resonances with a database
Separations of tags	0 mm	> 70 mm	Dependent on HPBW	Narrow
Data capacity	High (8 bits)	Low (3 bits)	High	Low (3 bits)
Need for calibration?	No	Yes	Yes	Yes
Hardware complexity	Medium	Low	High	Low
Test of reliability?	Yes	No	No	No

bands show limited improvements, whereas the fourth subfrequency band has an improvement of 7.9% for the result at $d = 0$ mm. As a read range of 200 mm is electrically larger for the fourth subfrequency band, this band has more noticeable errors. If an error correction code is implemented for the last digit [48], the detection reliability will be improved significantly, at the expanse of data capacity.

Although the proposed technique is majorly derived from ICA, two distinct features are added to serve the frequency-coded chipless RFID. First, the proposed technique integrates STFT to prevent performing an additional calibration for clutter. Second, the ICA framework is performed only subject to low SNR. This ensures superior performance compared to SDMA.

The characteristics of the multitag detection techniques for the frequency-coded chipless RFID are summarized in Table I. Compared to signal processing using TDoA and SDMA, the most distinguishing feature of the proposed technique is the minimum allowable separation of tags. The proposed technique depicts reliability of 80.4% even for immediately adjacent tags, whereas STMPM and SDMA show the reliability of 5.6% and 27.3%, respectively. Although the comparison of resonances with a database has the potential for overcoming this challenge, this method suffers from reduced data capacity due to low-frequency usage efficiency. Furthermore, the proposed technique is the first multitag detection method that integrates a calibration-free scheme. Although the proposed technique requires measuring multiple samples, the complexity of hardware architecture is lower than that of SDMA, as ICA does not require phased array technology or narrow HPBWs. Finally, the proposed technique is validated through not only several instances but also reliability in a statistical approach.

Although the proposed technique depicts these advantages, it also rises to several challenges. First, when the separation of tags increases, the orientation misalignment may cause frequency detuning for the backscattering signals. In this situation, the design of the system using cross-polarized encoding is not straightforward. The proposed technique may require the feature of orientation-insensitive and cross-polarization encoded chipless RFID [49]. Second, although the proposed SNR procedure, as expressed in (2), can identify whether collisions happen, this scheme has limitations if multiple tags have an identical ID. Third, the current version of ICA requires prior knowledge about the number of tags that collided. If the number of tags is different from that of measurements, the ICA needs to be adapted to these scenarios. This leads to the special forms of ICA known as undercomplete or overcomplete problems [39].

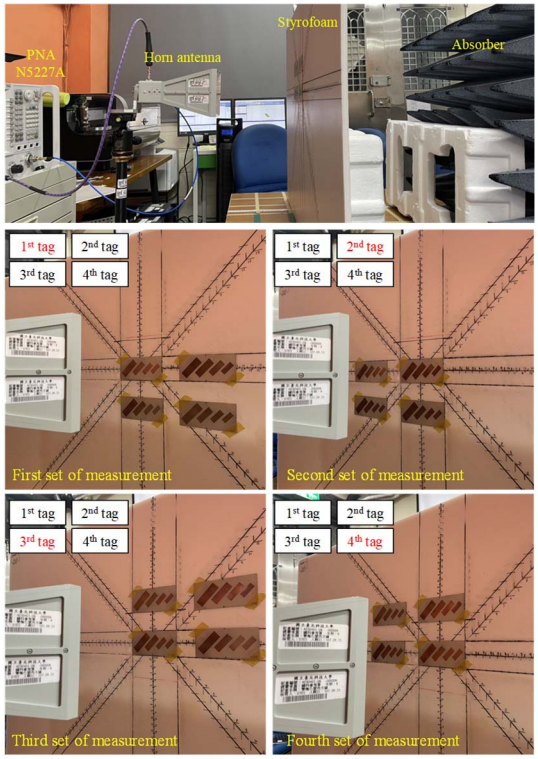

Fig. 26. Experimental setup for separating the mixing signals of four tags.

V. REAL-WORLD IMPLEMENTATION

The aforementioned results are achieved in an ideal environment. In a real-world implementation, the tags may depict orientation and polarization mismatch, and the positioning may depict a displacement. Also, more numbers of collided tags may be the case. These issues are discussed in this section.

A. Detection of Four Tags

Fig. 26 depicts the experimental setup for separating four collided backscattering signals. The arrangement shown in Fig. 12 is extended to collect four samples. Each sample is determined by measuring the backscattering fields from the phase center of a tag. The four samples are detected with an identical read range of 200 mm, whereas the separation of adjacent tags is 20 mm.

Four tags with IDs of 1003, 3122, 0312, and 2020 are selected to demonstrate the blind source separation. Without performing the ICA process, SDMA obtains RCS responses, as shown in Fig. 27. The four sets of measurements depict multiple peaks in each subfrequency band. In comparison with the scenario of two tags, the number of peaks increases in all subfrequency bands. SDMA outputs the results as 0313, 2022, 0313, and 3322, respectively. None of them are correct.

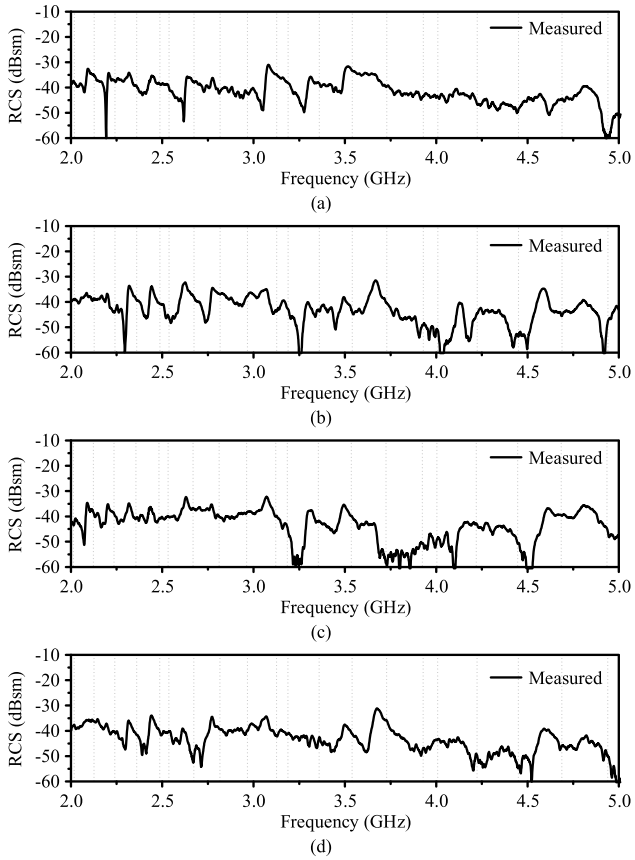

Fig. 27. Mixing backscattering signals as the horn antenna illuminates the phase center of (a) first, (b) second, (c) third, and (d) fourth tags.

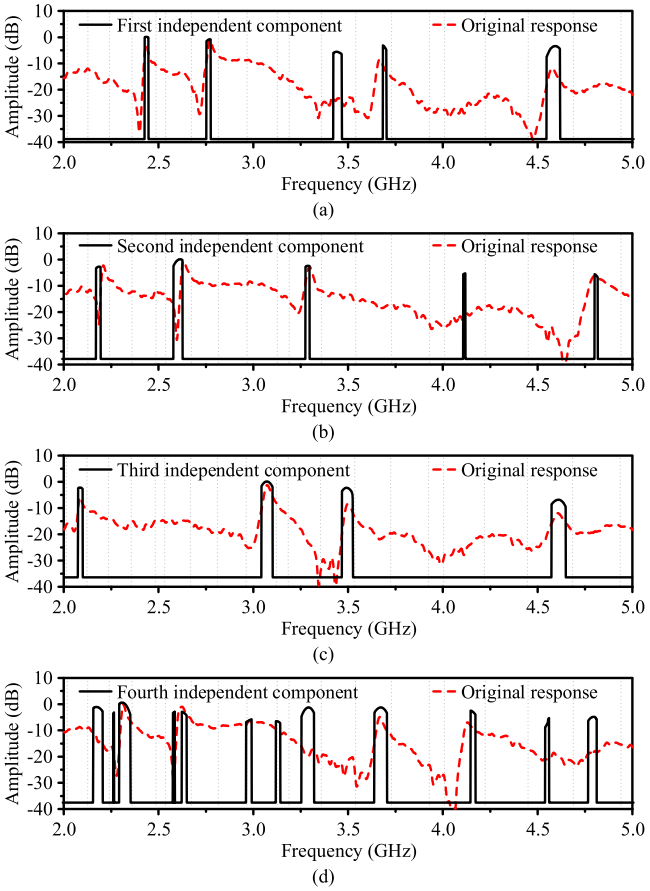

Fig. 28. Separated frequency signatures without performing calibration for the tags with IDs of (a) 3122, (b) 1003, (c) 0312, and (d) 2020.

The proposed technique is applied to the four mixing responses. During the process, the convergence is slower due to the increased number of decision variables. The Kurtosis reaches the maximum after the 20th iteration. The optimum weights for identifying the independent components are (18), as shown at the bottom of the page.

These optimum weights multiplied by the whitened mixtures result in the independent components. After performing the additional filtering for the time–frequency spectrograms, the estimation of the individual resonances is shown in Fig. 28. The IDs are decoded as 3122, 1003, 0312, and 2020, respectively, which agrees with the original ones.

However, the detection of four tags is more challenging than that of two tags. In Fig. 28(a), the tag with ID of 3122 encodes the third subfrequency band using the third frequency slot, whereas the first frequency slot also presents a local maximum. The magnitude of this local maximum is smaller than that at the third frequency slot, so the decoding still provides the correct estimation. When more numbers of mixture signals are to be addressed, the increasing complexity of the mixing matrix makes the blind source separation be sensitive to adjacent resonances, which further causes potential detection errors. Although the proposed technique shows successful signal separation in several instances, more studies are required to enhance the robustness of ICA for a large number of collided tags.

B. Orientation Mismatch

Next, we analyze the signal separation under orientation mismatch. Fig. 29 shows the illustration of the experiment. The experimental setup follows the description shown in Fig. 8. The two tags are selected as IDs of 0303 and 2210. While the first tag (ID: 0303) stays perfect orientation match with respect to the incident waves, the second tag (ID: 2210) is tilted side to side on the x-axis. The level of orientation is characterized by a roll angle, θ_r, sampled from $\theta_r = 0°$ to $\theta_r = 90°$ with incremental steps of 15°. The separation between the two tags is 45 mm, and the read range is 200 mm.

$$\tilde{\mathbf{w}} = \begin{bmatrix} -0.54 - j0.15 & -0.13 - j0.23 & 0.43 + j0.50 & 0.35 - j0.25 \\ 0.11 - j0.51 & -0.33 + j0.12 & -0.25 - j0.18 & -0.01 - j0.71 \\ -0.14 + j0.41 & 0.34 - j0.56 & -0.46 + j0.03 & -0.05 - j0.41 \\ -0.12 - j0.46 & 0.09 - j0.60 & 0.26 - j0.43 & -0.33 + j0.20 \end{bmatrix} \tag{18}$$

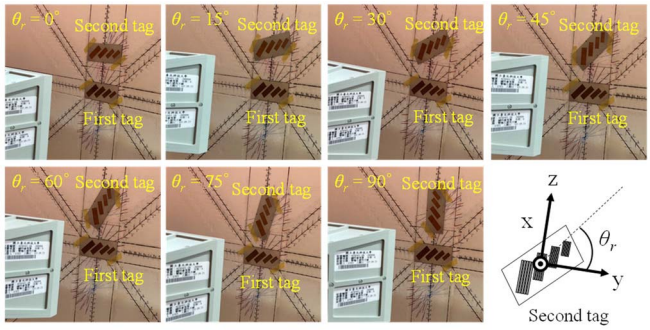

Fig. 29. Experimental setup for measuring the collided responses under orientation mismatch.

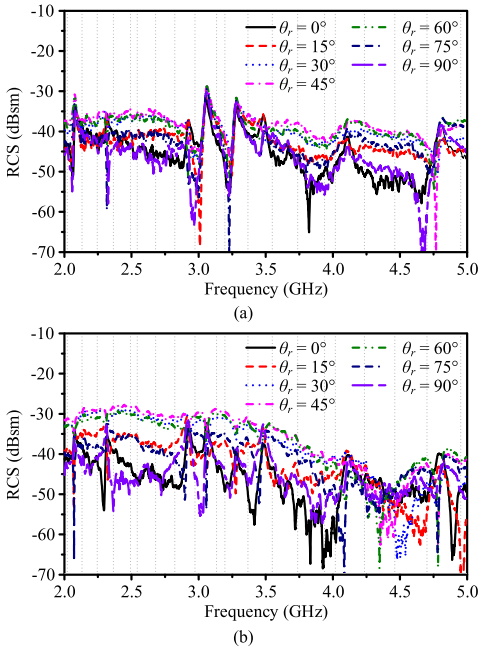

Fig. 30. Mixture RCS responses detected by SDMA as the horn antenna illuminates the tags with IDs of (a) 0303 and (b) 2210 under orientation mismatch.

Fig. 30 exhibits the mixture backscattering fields of the two samples. These RCS responses vary over θ_r. In particular, the second sample, obtained along the phase center of the second tag, exhibits more significant differences. Since the second tag is the one rotated in several angles, the distinction of results is stronger than that of the first sample.

These mixing backscattering fields are processed using the proposed technique, and the results are shown in Fig. 31. The ID of the first tag is successfully detected at $\theta_r = 0°$, $\theta_r = 15°$, $\theta_r = 30°$, $\theta_r = 75°$, and $\theta_r = 90°$, whereas that of the second tag can be uncovered only at $\theta_r = 0°$, $\theta_r = 15°$, $\theta_r = 75°$, and $\theta_r = 90°$. As θ_r approaches 45°, false resonances become more severe. For example, at $\theta_r = 45°$, the estimated independent components of the second tag are zero. No resonances can be uncovered.

Although the proposed technique cannot separate the mixture signals at $30° \leq \theta_r \leq 60°$, the underlying reason is the rotation of cross-polarized components, instead of the process of ICA. The resonator implemented is five thin strips oriented

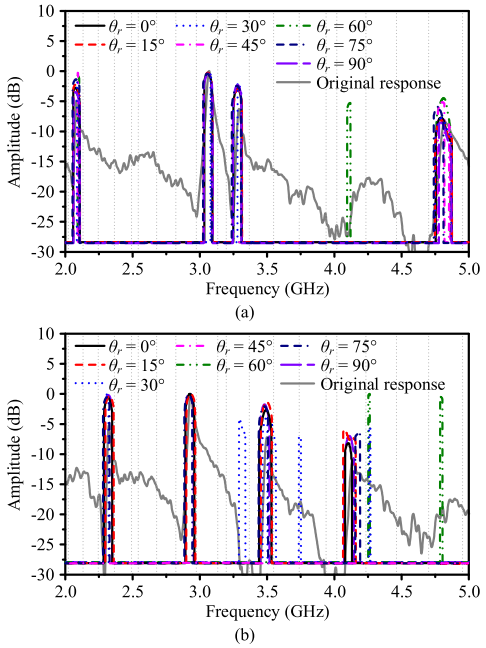

Fig. 31. Separated frequency signatures for the tags with IDs of (a) 0303 and (b) 2210 under orientation mismatch.

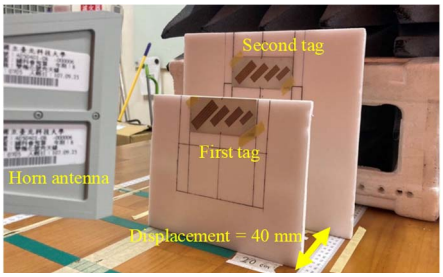

Fig. 32. Experimental setup for measuring collided backscattering signals with different powers.

at 45° and backed with the conductor. When the 45°-oriented strip is rotated by another 45°, these strips become parallel to the *z*-axis, which minimizes the cross-polarized components. In this case, the resonances encoded are naturally undetectable even for one single tag. Since the backscattering fields that input the ICA algorithm are already distorted, it is reasonable that the IDs cannot be found around $\theta_r = 45°$. Nevertheless, the proposed technique demonstrates successful interrogation against $0° \leq \theta_r \leq 15°$ and $75° \leq \theta_r \leq 90°$. If the orientation angle can be controlled within these ranges, the frequency shift is tolerable in the frequency slot, and ICA is still capable of blind source separation.

C. Displacement of Tags

Finally, the effect of a displacement of tags is analyzed. Fig. 32 illustrates the experimental setup, where a horizontal displacement of 40 mm is manipulated to create unequal read ranges and backscattering power. The IDs of the tags are selected as 2001 and 3320. The vertical separation between tags is 20 mm, whereas the read ranges of the two mixture samples are 200 and 240 mm, respectively.

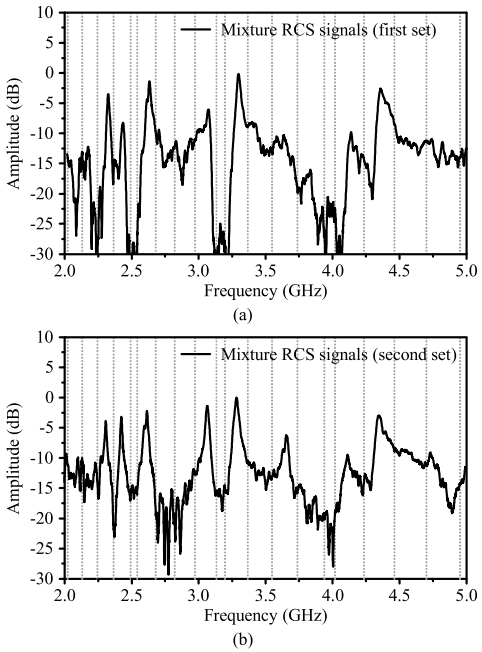

Fig. 33. Mixture RCS responses detected by SDMA as the horn antenna illuminates the tags with IDs of (a) 2001 and (b) 3320 under a displacement of 40 mm.

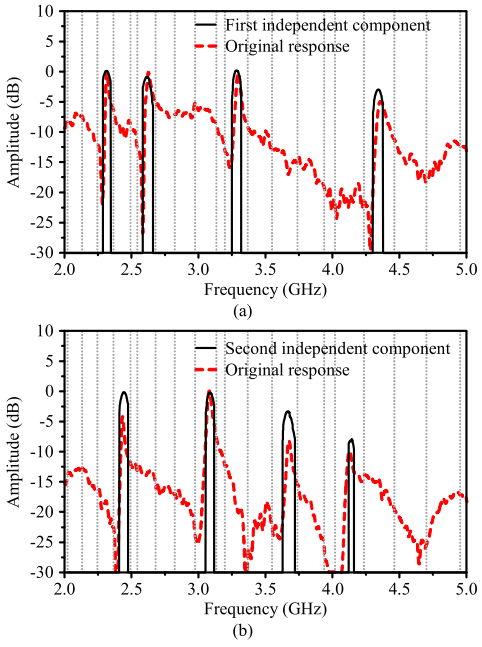

Fig. 34. Separated frequency signatures for the tags with IDs of (a) 2001 and (b) 3320 under a displacement of 40 mm.

Such mixture RCS responses are shown in Fig. 33. The results of SDMA still depict multiple and confounding peaks. In comparison with the case without the displacement (see Fig. 11), the second mixture RCS signals exhibit the resonances from the first tag more significantly. In the third subfrequency band, both samples depict a significant resonance at the first frequency slot, which is derived from the first tag (ID: 20"0"1); similarly, in the fourth subfrequency band, both samples show a significant resonance at the second frequency slot, which also belongs to the first tag (ID: 200"1"). Thus, the SDMA cannot identify the correct IDs with a displacement considered.

Processed by the proposed technique, the mixing data are converted into individual responses, as shown in Fig. 34. The IDs are successfully retrieved even though the first tag depicts stronger backscattering power. Considering the second tag, which shows a longer read range of 240 mm, the third and fourth resonances are uncovered by means of maximizing the Kurtosis. This further indicates that ICA provides robust performance under unequal backscattering power and a displacement between tags.

VI. Conclusion

A multitag detection technique has been presented for the frequency-coded chipless RFID to achieve minimum permissible separations of tags, high data capacity, calibration-free feature, and reduced hardware complexity from SDMA. The theory and procedure are explained in detail, and the capability is validated through the 8 bit system in terms of reliability. The results show that the proposed technique achieves reliability of 80.4%–91.5% when two tags are separated by 0–30 mm. In contrast, signal processing using STMPM and SDMA demonstrates the reliability of 4.3%–8.2% and 27.3%–55.6%, respectively. Furthermore, improving reliability is obtained without performing additional measurements for calibration. These results are helpful for advancing chipless RFID toward real-world, multitag, and item-level tagging. Our future work is in-depth hardware and software development for the ICA framework, including broadband and pattern-reconfigurable antennas serving the reader and the undercomplete and overcomplete versions for the ICA algorithm.

References

[1] S. K. Behera and N. C. Karmakar, "Chipless RFID printing technologies: A state of the art," *IEEE Microw. Mag.*, vol. 22, no. 6, pp. 64–81, Jun. 2021.

[2] V. Sharma and M. Hashmi, "Advances in the design techniques and applications of chipless RFIDs," *IEEE Access*, vol. 9, pp. 79264–79277, 2021.

[3] M. E. B. Jalil *et al.*, "High capacity and miniaturized flexible chipless RFID tag using modified complementary split ring resonator," *IEEE Access*, vol. 9, pp. 33929–33943, 2021.

[4] R. Raju, G. E. Bridges, and S. Bhadra, "Wireless passive sensors for food quality monitoring: Improving the safety of food products," *IEEE Antennas Propag. Mag.*, vol. 62, no. 5, pp. 76–89, Oct. 2020.

[5] A. Ramos, Z. Ali, A. Vena, M. Garbati, and E. Perret, "Single-layer, flexible, and depolarizing chipless RFID tags," *IEEE Access*, vol. 8, pp. 72929–72941, 2020.

[6] S. Deif and M. Daneshmand, "Multiresonant chipless RFID array system for coating defect detection and corrosion prediction," *IEEE Trans. Ind. Electron.*, vol. 67, no. 10, pp. 8868–8877, Oct. 2020.

[7] M. El-Absi, A. A.-H. Abbas, A. Abuelhaija, K. Solbach, and T. Kaiser, "Chipless RFID infrastructure based self-localization: Testbed evaluation," *IEEE Trans. Veh. Technol.*, vol. 69, no. 7, pp. 7751–7761, Jul. 2020.

[8] K. R. Brinker, M. Vaccaro, and R. Zoughi, "Application-adaptable chipless RFID tag: Design methodology, metrics, and measurements," *IEEE Trans. Instrum. Meas.*, vol. 69, no. 6, pp. 3882–3895, Jun. 2020.

[9] K. Suresh, V. Jeoti, S. Soeung, M. Drieberg, M. Goh, and M. Z. Aslam, "A comparative survey on silicon based and surface acoustic wave (SAW)-based RFID tags: Potentials, challenges, and future directions," *IEEE Access*, vol. 8, pp. 91624–91647, 2020.

[10] F. Paredes, C. Herrojo, R. Escude, E. Ramon, and F. Martin, "High data density near-field chipless-RFID tags with synchronous reading," *IEEE J. Radio Freq. Identificat.*, vol. 4, no. 4, pp. 517–524, Dec. 2020.

[11] M. Garbati, E. Perret, R. Siragusa, and C. Halope, "Ultrawideband chipless RFID: Reader technology from SFCW to IR-UWB," *IEEE Microw. Mag.*, vol. 20, no. 6, pp. 74–88, Jun. 2019.

[12] J. J. Martinez-Martinez, F. J. Herraiz-Martinez, and G. Galindo-Romera, "A contactless RFID system based on chipless MIW tags," *IEEE Trans. Antennas Propag.*, vol. 66, no. 10, pp. 5064–5071, Oct. 2018.

[13] S. Genovesi, F. Costa, A. Monorchio, and G. Manara, "Chipless RFID tag exploiting multifrequency delta-phase quantization encoding," *IEEE Antennas Wireless Propag. Lett.*, vol. 15, pp. 738–741, 2015.

[14] O. Rance, E. Perret, R. Siragusa, and P. Lemaitre-Auger, "Effect of distance for chipless RFID magnitude coding," *IEEE J. Radio Freq. Identificat.*, vol. 3, no. 2, pp. 77–82, Jun. 2019.

[15] C. Feng, W. Zhang, L. Li, L. Han, X. Chen, and R. Ma, "Angle-based chipless RFID tag with high capacity and insensitivity to polarization," *IEEE Trans. Antennas Propag.*, vol. 63, no. 4, pp. 1789–1797, Apr. 2015.

[16] S. Harma, W. G. Arthur, C. S. Hartmann, R. G. Maev, and V. P. Plessky, "Inline SAW RFID tag using time position and phase encoding," *IEEE Trans. Ultrason., Ferroelectr., Freq. Control*, vol. 55, no. 8, pp. 883–889, Aug. 2008.

[17] L. Arjona, H. Landaluce, A. Perallos, and E. Onieva, "Timing-aware RFID anti-collision protocol to increase the tag identification rate," *IEEE Access*, vol. 6, pp. 33529–33541, 2018.

[18] J. Shin, B. Jeon, and D. Yang, "Multiple RFID tags identification with M-ary query tree scheme," *IEEE Commun. Lett.*, vol. 17, no. 3, pp. 604–607, Mar. 2013.

[19] R. Rezaiesarlak and M. Manteghi, "A space-time-frequency anticollision algorithm for identifying chipless RFID tags," *IEEE Trans. Antennas Propag.*, vol. 62, no. 3, pp. 1425–1432, Mar. 2014.

[20] R. Rezaiesarlak and M. Manteghi, "Accurate extraction of early-/late-time responses using short-time matrix pencil method for transient analysis of scatterers," *IEEE Trans. Antennas Propag.*, vol. 63, no. 11, pp. 4995–5002, Nov. 2015.

[21] R. Rezaiesarlak and M. Manteghi, "A new anti-collision algorithm for identifying chipless RFID tags," in *Proc. Antennas Propag. Soc. Int. Symp.*, 2013, pp. 1722–1723.

[22] B. Lopes, T. Varum, and J. N. Matos, "Use of FrFT in an indoor scenario for chipless RFID tags ID recovery," *IET Microw., Antennas Propag.*, vol. 14, no. 12, pp. 1316–1322, Oct. 2020.

[23] R. Azim and N. Karmakar, "A collision avoidance methodology for chipless tags," in *Proc. IEEE Asia–Pacific Microw. Conf.*, Melbourne, VIC, Australia, Dec. 2011, pp. 1514–1517.

[24] Z. Li, Y. Lan, G. He, S. He, and S. Wang, "Chipless RFID tag anti-collision algorithm based on FRactional Fourier transform," in *Proc. Chin. Automat. Congr. (CAC)*, Xi'an, China, Nov. 2018, pp. 2979–2984.

[25] Z. Li, Y. Lan, G. He, S. He, and S. Wang, "Optimal window fractional Fourier transform based chipless RFID tag anti-collision algorithm," in *Proc. Chin. Autom. Congr. (CAC)*, Xi'an, China, Nov. 2018, pp. 4237–4242.

[26] C. D. R. Lopes, E. C. Gurjão, and F. M. de Assis, "Optimized recovery of collided chipless RFID signals using fractional Fourier transform," in *Proc. IEEE RFID Technol. Appl. Conf.*, Tampere, Finland, Sep. 2014, pp. 91–96.

[27] R.-E.-A. Anee and N. C. Karmakar, "Anti-collision methods for chipless RFID systems," in *Proc. Asia–Pacific Microw. Conf. (APMC)*, Nanjing, China, Dec. 2015, pp. 1–3.

[28] R. Anee and N. C. Karmakar, "Efficient collision detection method in chipless RFID systems," in *Proc. 7th Int. Conf. Electr. Comput. Eng.*, Dhaka, Bangladesh, Dec. 2012, pp. 830–833.

[29] M. Barahona, D. Betancourt, and F. Ellinger, "Using UWB IR radar technology to decode multiple chipless RFID tags," in *Proc. IEEE Int. Conf. Ubiquitous Wireless Broadband*, Nanjing, China, Oct. 2016, pp. 1–6.

[30] R. E. Azim, N. C. Karmakar, and E. Amin, "Short time Fourier transform (STFT) for collision detection in chipless RFID systems," in *Proc. Int. Symp. Antennas Propag.*, Hobart, TAS, Australia, Nov. 2015, pp. 1–4.

[31] M. El-Hadidy, A. El-Awamry, A. Fawky, M. Khaliel, and T. Kaiser, "Real-world testbed for multi-tag UWB chipless RFID system based on a novel collision avoidance MAC protocol," *Trans. Emerg. Telecommun. Technol.*, vol. 27, no. 12, pp. 1707–1714, Dec. 2016.

[32] M. El-Hadidy, A. El-Awamry, A. Fawky, M. Khaliel, and T. Kaiser, "A novel collision avoidance MAC protocol for multi-tag UWB chipless RFID systems based on notch position modulation," in *Proc. 9th Eur. Conf. Antennas Propag. (EuCAP)*, Lisbon, Portugal, Apr. 2015, pp. 1–5.

[33] A. El-Awamry, M. Khaliel, A. Fawky, M. El-Hadidy, and T. Kaiser, "Novel adaptive sliding window algorithm reducing latency for multi-tag chipless RFID systems," in *Proc. USNC-URSI Radio Sci. Meeting*, Vancouver, BC, Canada, Jul. 2015, p. 1.

[34] Z. Li, Y. Lan, G. He, S. He, and S. Wang, "Chipless RFID tag anti-collision algorithm based on successive approximation comparative amplitude coding," in *Proc. Chin. Autom. Congr.*, Xi'an, China, Nov. 2018, pp. 2396–2401.

[35] A. El-Awamry, M. Khaliel, A. Fawky, and T. Kaiser, "A novel multi-tag identification technique for frequency coded chipless RFID systems based on look-up-table approach," in *Proc. 11th Eur. Conf. Antennas Propag. (EUCAP)*, Paris, France, Mar. 2017, pp. 2070–2074.

[36] J. G. D. Hester and M. M. Tentzeris, "Inkjet-printed flexible mm-wave Van-Atta reflectarrays: A solution for ultralong-range dense multitag and multisensing chipless RFID implementations for IoT smart skins," *IEEE Trans. Microw. Theory Techn.*, vol. 64, no. 12, pp. 4763–4773, Dec. 2016.

[37] M. Khaliel, A. El-Awamry, A. Fawky, and T. Kaiser, "Long reading range chipless RFID system based on reflectarray antennas," in *Proc. 11th Eur. Conf. Antennas Propag. (EUCAP)*, Paris, France, Mar. 2017, pp. 1–5.

[38] N. C. Karmakar, "Optical beamforming phased arrays for UWB chipless RFID reader," *Handbook of Smart Antennas for RFID System*. New York, NY, USA: Wiley, 2010, pp. 243–281.

[39] G. R. Naik and D. K. Kumar, "An overview of independent component analysis and its applications," *Informatica*, vol. 35, no. 1, pp. 63–81, 2011.

[40] A. Vena, E. Perret, and S. Tedjni, "A depolarizing chipless RFID tag for robust detection and its FCC compliant UWB reading system," *IEEE Trans. Microw. Theory Techn.*, vol. 61, no. 8, pp. 2982–2994, Aug. 2013.

[41] J.-A. Lin, J.-Y. Jhang, F.-P. Lai, B.-L. Lin, Y.-M. Jhang, and Y.-S. Chen, "Analysis of calibration-free detection techniques for frequency-coded chipless RFID," *IEEE Trans. Antennas Propag.*, vol. 69, no. 3, pp. 1681–1691, Mar. 2021.

[42] Y. Chen, T. Jiang, and F. Lai, "Design rule development for frequency-coded chipless radiofrequency identification with high capacity," *IET Microw., Antennas Propag.*, vol. 13, no. 8, pp. 1255–1261, Jul. 2019.

[43] A. Hyvarinen, "One-unit contrast functions for independent component analysis: A statistical analysis," in *Proc. Neural Netw. Signal Process. IEEE Signal Process. Soc. Workshop*, Amelia Island, FL, USA, Sep. 1997, pp. 388–397.

[44] E. Bingham and A. Hyvärinen, "A fast fixed-point algorithm for independent component analysis of complex valued signals," *Int. J. Neural Syst.*, vol. 10, no. 1, pp. 1–8, Feb. 2000.

[45] Y.-H. Cho, F.-P. Lai, and Y.-S. Chen, "Orientation-insensitive chipless RFID achieved in multiple rotational degrees of freedom," *IEEE Trans. Antennas Propag.*, early access, Jan. 28, 2022, doi: 10.1109/TAP.2022.3145446.

[46] M. Forouzandeh and N. Karmakar, "Self-interference cancelation in frequency-domain chipless RFID readers," *IEEE Trans. Microw. Theory Techn.*, vol. 67, no. 5, pp. 1994–2009, May 2019.

[47] J. Aliasgari, M. Forouzandeh, and N. Karmakar, "Chipless RFID readers for frequency-coded tags: Time-domain or frequency-domain?" *IEEE J. Radio Freq. Identificat.*, vol. 4, no. 2, pp. 146–158, Jun. 2020.

[48] G. Khadka, M. S. Arefin, and N. C. Karmakar, "Using punctured convolution coding (PCC) for error correction in chipless RFID tag measurement," *IEEE Microw. Wireless Compon. Lett.*, vol. 30, no. 7, pp. 701–704, Jul. 2020.

[49] N. Barbot, O. Rance, and E. Perret, "Chipless RFID reading method insensitive to tag orientation," *IEEE Trans. Antennas Propag.*, vol. 69, no. 5, pp. 2896–2902, May 2021.

Wen-Sen Li was born in Taipei, Taiwan, in 1996. He received the B.S. degree in electronic engineering from Chung Yuan Christian University, Taoyuan, Taiwan, in 2019, and the M.S. degree in electronic engineering from the National Taipei University of Technology (NTUT), Taipei, in 2021.

He participated in the Einstein Program for the EM Optimization Laboratory, NTUT, focusing on multitag detection and anticollision algorithms. His research interests include chipless radio frequency identification (RFID), signal processing, the design of antennas and radio frequency (RF) resonators, and system integration.

Cong-Zhi Peng was born in Hsinchu, Taiwan, in 1998. He received the B.S. degree in electrical engineering from Feng Chia University, Taichung, Taiwan, in 2020. He is currently pursuing the M.S. degree in electronic engineering with the National Taipei University of Technology (NTUT), Taipei, Taiwan.

His current research interests include chipless radio frequency identification (RFID) and signal processing.

Fei-Peng Lai was born in Chiayi, Taiwan. She received the B.S. degree in electronic engineering from the National Taipei University of Technology, Taipei, Taiwan, in 2017, where she is currently pursuing the Ph.D. degree in electronic engineering.

She has participated in numerous research projects, including 60 GHz on-chip antennas from KaiKuTek, Taipei, and chipless RFID development from the Ministry of Science and Technology, Taiwan. Her current research interests include chipless radio frequency identification (RFID), antennas, and wireless communications.

Ms. Lai has served on the Reviewer Board for the IEEE ACCESS.

Pin-Sung Lai was born in Taichung, Taiwan, in 1995. He received the B.S. degree in electronic engineering from the National Taipei University of Technology (NTUT), Taipei, Taiwan, in 2021.

He joined the EM Optimization Laboratory, NTUT, for the period 2019–2021. His research interests include system integration, firmware development, and statistical analysis of engineering data.

Yen-Sheng Chen (Member, IEEE) was born in Taichung, Taiwan. He received the B.S. degree in electrical engineering and the M.S. and Ph.D. degrees in communication engineering from National Taiwan University, Taipei, Taiwan, in 2007, 2009, and 2012, respectively.

Since 2013, he has been a Faculty Member with the Department of Electronic Engineering, National Taipei University of Technology (NTUT), Taipei, where he is currently a Professor. He has participated in a wide range of research projects, including chipless radio frequency (RF) identification, transparent antennas and metasurfaces, mm-wave antennas and circuits, RF energy harvesting, antenna array failure correction, antennas for body-centric communications, microwave reconfigurable components, and multiobjective optimization techniques. His recent research interests include chipless sensor networks, high-gain antennas, and inkjet printing technology.

Dr. Chen was a recipient of the Outstanding Reviewers Award from the IEEE Antennas and Wireless Propagation Letters for the period 2017–2021, the Outstanding Reviewers Award from the IEEE Transactions on Antennas and Propagation in 2019 and 2020, the Future Tech Award from the Ministry of Science and Technology, Taiwan, in 2021, the Outstanding Research Award from NTUT in 2019, the Dr. Shechtman Young Researcher Award from NTUT in 2018, the Outstanding Research Award from the College of Electrical Engineering and Computer Science (EECS), NTUT, in 2018 and 2019, and the Remarkable Teaching Award from the College of EECS, NTUT, in 2020. He was the General Secretariat and the Publication Chair of the ISAP 2021 Symposium and a Guest Editor of *IEICE Communications Express* in 2022. He has served on the editorial/review boards for many technical journals, transactions, proceedings, and letters.